The Atmospheric Hydrologic Cycle over the Arctic Basin from Reanalyses. Part II: Interannual Variability*

ARIC N. ROGERS,+ DAVID H. BROMWICH,# AND ELIZABETH N. SINCLAIR

Polar Meteorology Group, Byrd Polar Research Center, The Ohio State University, Columbus, Ohio

RICHARD I. CULLATHER

Department of Aerospace Engineering Sciences, University of Colorado, Boulder, Colorado

(Manuscript received 14 February 2000, in final form 20 September 2000)

ABSTRACT

Previously, the atmospheric moisture budgets over the Arctic Basin as represented by reanalysis data from the National Centers for Environmental Prediction–National Center for Atmospheric Research (NCEP–NCAR) reanalysis and from the European Centre for Medium-Range Weather Forecasts reanalysis were evaluated for the overlap period of 1979–93 and found to be very similar to each other and to the available observations. Here emphasis is on the 50 yr of the NCEP–NCAR reanalysis (January 1949–May 1999) to depict the interannual variability of the atmospheric moisture fluxes across 70°N and their convergence farther north.

Precipitation minus evaporation ($P - E$) calculated from moisture flux convergence is compared with three large-scale circulation patterns that strongly affect the interannual variability of $P - E$ over the Arctic and its environs: the North Atlantic oscillation (NAO), the Arctic oscillation (AO), and the North Pacific oscillation (NPO). The impact of the NAO and the closely related AO on Arctic Basin $P - E$ is found to be marked, with a $P - E$:NAO winter correlation of 0.49 (0.56 for the AO). On an annual basis, Arctic Basin $P - E$ is much more closely correlated with the NAO (0.69) than with the AO (0.49), consistent with the Atlantic Ocean domination of the northward poleward moisture flux across 70°N. Regional analysis confirms that the NAO impact on $P - E$ is concentrated around the periphery of the North Atlantic Ocean and extends north into the Arctic Ocean during winter. The NAO and AO differ in their $P - E$ modulation over the northern Eurasia sector with the AO being much more important for all seasons except summer (winter AO:$P - E$ correlation 0.53, NAO:$P - E$ correlation 0.16), consistent with its much stronger impact on the atmospheric circulation in that area. The NPO was associated with a much more modest modulation of Arctic Basin $P - E$ (winter correlation of 0.33 and annual value of 0.10), with its regional signal being strongest over Alaska, northwestern Canada, and areas to the north. About 40% of the interwinter variance of $P - E$ over the sector that includes northeastern Canada is linked with the combined influence of the NAO–AO and NPO.

A region of large poleward moisture transport variability during summer was previously identified over western Siberia, east of the Urals, associated with the development of the Urals trough. Here it is shown that this is due to an opposing circulation pattern, with high (low) poleward moisture transport over the west Siberian plain during low (high) poleward moisture transport over Scandinavia. A pronounced trough–ridge pattern accompanies this circulation regime that is primarily confined to July. Because the summer moisture transport dominates the annual total for this region, these circulation patterns produce this area's large interannual poleward moisture transport variability.

1. Introduction

Precipitation plays a primary role in the hydrologic budget of the Arctic Basin. Variations in Arctic precipitation directly and indirectly (e.g., through river runoff) affect ocean salinity and ice conditions that in turn impact the net flow of freshwater and ice from this region through the Fram Strait and Greenland Sea into the North Atlantic Ocean. The degree of freshening of high-latitude North Atlantic surface waters impacts the global thermohaline circulation, which can potentially have a significant impact on the climate system (Broecker 1997). The dominant atmospheric variability pattern in the North Atlantic region is the North Atlantic oscillation (NAO; van Loon and Rogers 1978), which is very similar to, but less comprehensive than, the Arctic oscillation (AO); (Thompson and Wallace 1998). This mass oscillation between the subpolar low near Iceland and the subtropical high near the Azores enhances the

* Byrd Polar Research Center Contribution Number 1189.

+ Current affiliation: Molecular and Cellular Biology Department, University of Massachusetts, Amherst, Massachusetts.

Additional affiliation: Atmospheric Sciences Program, Department of Geography, The Ohio State University, Columbus, Ohio.

Corresponding author address: David H. Bromwich, Polar Meteorology Group, Byrd Polar Research Center, The Ohio State University, 1090 Carmack Road, Columbus, OH 43210-1002.
E-mail: bromwich@polarmet1.mps.ohio-state.edu

westerlies during a positive NAO phase. Serreze et al. (1997) found that a more positive NAO index in recent years has been associated with a significant increase in cyclones north of 60°N. This trend was very noticeable over the central Arctic Ocean, where it was associated with a decrease in high-latitude sea level pressure of up to 4 hPa and also with recent changes in sea-ice conditions and surface temperatures. Overpeck et al. (1997) showed that the variability seen in a 400-yr compilation of Arctic surface temperature proxies may be connected to decadal-scale variability in phenomena such as the NAO and the themohaline circulation. This arises because temperature is closely tied to atmospheric moisture transport via cyclonic activity (Maslanik et al. 1996) and to regional sea-ice variations (Chapman and Walsh 1993). In order to evaluate the degree to which large-scale atmospheric patterns are related to Arctic Basin precipitation, it is necessary to find a suitable precipitation dataset. To this end, we briefly summarize the earlier portion of this research.

In Cullather et al. (2000), computed and forecast precipitation from atmospheric reanalyses were compared with available observations and previous studies to assess the potential for using these numerical data in high–northern latitude precipitation studies. The reanalyses considered were the European Centre for Medium-Range Weather Forecasts 15-yr reanalysis (ERA-15; Gibson et al. 1997) and the collaborative reanalysis effort of the National Centers for Environmental Prediction–National Center for Atmospheric Research (NCEP–NCAR; Kalnay et al. 1996). It was found that moisture flux convergence (MFC), which is equal to precipitation − evaporation/sublimation ($P - E$) via atmospheric moisture budget, provided the best overall depiction of Arctic Basin precipitation. The MFC is computed from winds and moisture data from zero-hour analyses. Therefore, MFC is more representative of the observations than are the forecast precipitation and evaporation variables available from the reanalysis datasets, which result from a short-term model forecast. The period of the ERA-15 (1979–93) was looked at extensively in both reanalysis datasets; these are very similar to each other, and in general closely approximate the available observations. Here, we focus on the NCEP–NCAR reanalysis data that begin in January of 1949 and extend through May of 1999 (at the time of analysis), and we emphasize the moisture flux across 70°N that is well constrained by the radiosonde observations.

In addition to the effects of the NAO–AO (section 3), we also evaluate the impact of the North Pacific oscillation (NPO) on Arctic precipitation. In section 4, an assessment is made of the regional (interannual) variations of moisture flux across 70°N. This section features the general characteristics of these variations over the past 50 yr and takes a closer look at the variability over western Siberia, a region characterized by very high interannual variability in moisture flux across 70°N.

2. Data and methods

Reanalysis products have great potential for climate studies due to the consistent assimilation procedures and maximum observation usage employed during their creation. The NCEP–NCAR reanalysis dataset consists of analyses that are available four times daily, with T62 horizontal resolution (equivalent horizontal resolution of 200 km) and 28 sigma levels in the vertical. The data used in this study were obtained from NCAR at 2.5° × 2.5° horizontal resolution. Vertically, data were obtained at near-surface and standard pressure levels from January of 1949 to May of 1999.

A discussion of MFC calculations is given in Part I of the current study (Cullather et al. 2000) and more extensively discussed in earlier studies of MFC over Antarctica (Cullather et al. 1998). Arctic Basin time series of MFC are calculated using advection of water vapor and include local storage changes for all seasonally based time series. Monthly mean vertically integrated moisture fluxes used here are derived directly from the archived monthly NCEP–NCAR reanalysis dataset. These vertically integrated moisture fluxes are calculated directly from sigma coordinates and so do not suffer from mass balance errors that can arise during the conversion to archived pressure level data. However for completeness, a mass balance correction to the calculations of $P - E$ from MFC (cf. Goeber et al. 2000) is applied to the mean integrated moisture transports following Alestalo (1983). This correction has negligible impact on the long-term annual $P - E$ for the Arctic Basin, but can change the values for individual sectors (introduced later) by up to ±20%. In addition, the correction does not significantly alter the temporal variability of $P - E$ calculated without a mass balance correction.

Although reanalyses datasets are theoretically preferred for many climatological studies, a great deal of time and effort is spent producing them and it is understandable that perfection would not be attained at the first attempt. Part I of this study examines in depth the reanalysis shortcomings at high–northern latitudes, which are briefly summarized here. The NCEP–NCAR reanalyses were not produced using interannually varying snow cover for the period 1974–94. Also, the NWP model's horizontal diffusion parameterization is oversimplified, causing a high-latitude spurious wave pattern in the forecast P and E fields. The NCEP–NCAR reanalyses produce too much convective precipitation over land areas in summer. In a study by Serreze and Hurst (2000), NCEP–NCAR forecast P values were compared with an improved gauge-based climatology and were found to underestimate annual values over the Atlantic side of the Arctic. In addition, the current study includes data going back to 1949. These early data pre-

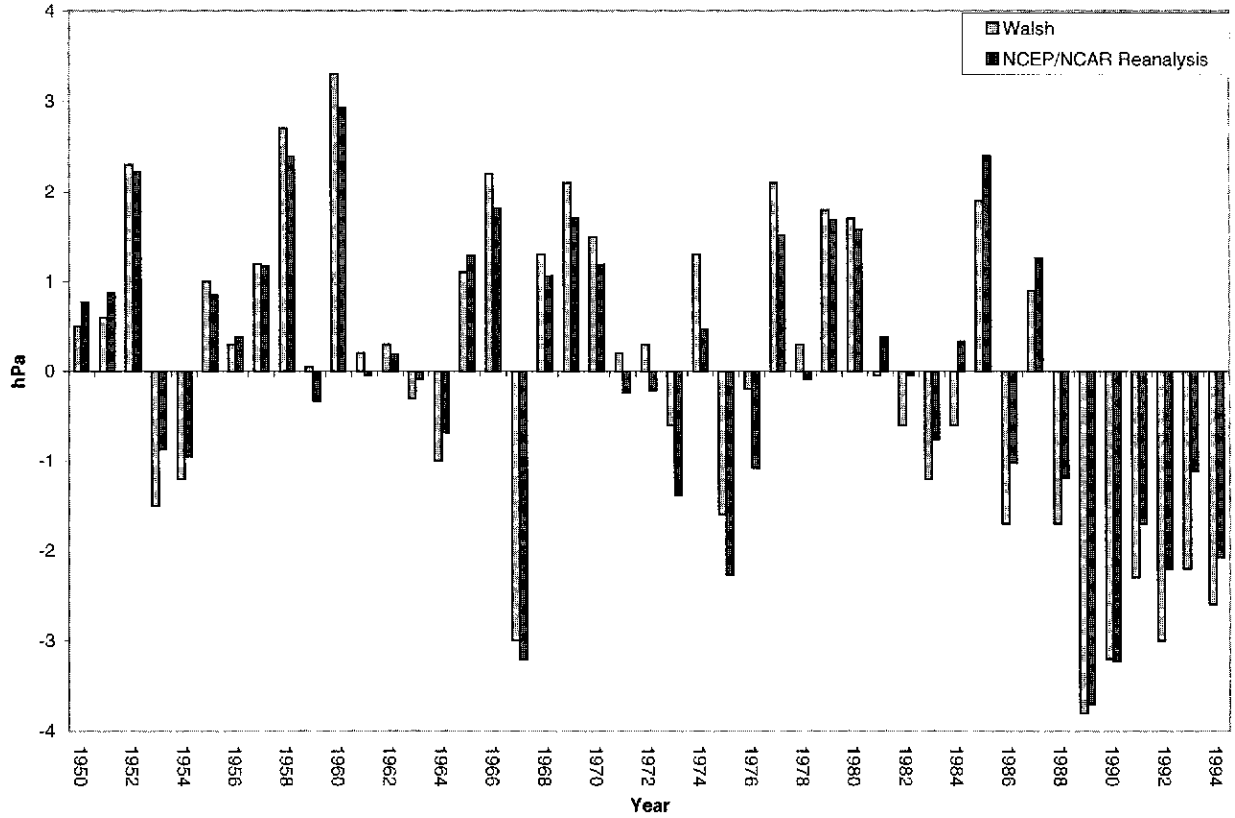

FIG. 1. Time series of annual area-averaged (70°–90°N) sea level pressure from observations [dark shaded bars, data from Fig. 5b of Walsh et al. (1996)] and NCEP–NCAR reanalysis (light bars). Anomalies are based on the period of overlap for the two series (1950–94).

date the satellite era and the Arctic drifting buoy network by as much as three decades. However, despite these obstacles, the 50+ yr of NCEP–NCAR reanalyzed data appear to accurately capture the annual changes in average Arctic Basin surface pressure when compared with annually averaged, observationally based values from Walsh et al. (1996), which date back to 1950 (Fig. 1) (correlation between the two series is 0.96, statistically significant at greater than the 99.5% confidence level). The mean pressure characteristics are very important to sector MFC computations, because they are directly linked to the atmospheric circulation and thus moisture transport in and around the Arctic Basin.

The other important factor in MFC calculations besides flow characteristics is atmospheric moisture content. The previous study by Serreze and Hurst (2000) of NCEP–NCAR reanalysis data reveals low-level moisture biases in the NCEP–NCAR reanalysis data for certain high-latitude land regions during summer. A consequence of this bias is too much convective precipitation in these areas. One region of focus is bounded by 60°–70°N and 120°–150°E (see their Table 1) for the period 1979–87. The problem is greatest at the 1000-hPa level, where regionally averaged reanalysis specific humidity values are too large when compared with data from three upper-air stations in the region, all of which are located near the 1000-hPa level. Fortunately, much of the low-level reanalysis data used in the comparison is aphysical, not incorrect. Both the Verkhoyanskiy ad Cherskogo mountain ranges are within this region. The average reanalysis surface pressure is less than 950 hPa. Further inspection reveals that, in general, the highest 1000-hPa specific humidity values are those that are the farthest below model topography. In Fig. 2, the average July (1979–87) meridional moisture flux (meridional wind multiplied by specific humidity) profile is plotted by pressure level for three upper-air stations in the regions—Zhigansk (66.76°N, 123.40°E), Zyrianka (65.73°N, 150.89°E), and Verkhoyansk (67.55°N, 133.38°E). The station data were obtained from the Historical Arctic Rawinsonde Archive of the National Snow and Ice Data Center (Serreze et al. 1992). Although there is a fourth upper-air station, Cokurdah (70.62°N, 147.88°E), that borders the region, there were almost no data available from this station for the period of interest. Included in the plots are the nearest NCEP–NCAR reanalysis gridpoint values of meridional moisture flux. Zhigansk most closely matches the reanalysis data, with the surface meridional moisture flux approximately the same and the profiles mirroring each other throughout the troposphere (Fig. 2a). At Zyrianka (Fig. 2b), the meridional moisture flux is not as close near

TABLE 1. Correlation analysis between annual and seasonal $P - E$ vs the NAO, AO, and NPO indices. Correlations greater than 0.40 are statistically significant at greater than the 99% confidence level.

	Basin	A	B	C	D	E	F
NAO–AO							
Annual	0.69/0.49	0.40/0.37	−0.04/0.16	0.19/0.42	0.38/0.28	0.13/0.08	0.59/0.11
Autumn	0.49/0.36	0.34/0.31	0.20/0.29	0.10/0.41	−0.11/0.16	−0.21/−0.09	0.59/−0.04
Winter	0.49/0.56	0.46/0.63	0.40/0.30	0.16/0.53	0.16/0.28	−0.53/−0.31	0.31/0.04
Spring	0.42/0.57	0.39/0.34	−0.03/0.33	0.12/0.47	0.21/0.35	−0.05/0.10	0.35/−0.08
Summer	0.29/0.56	0.02/0.36	−0.20/0.08	−0.22/−0.17	0.31/0.29	0.36/0.57	0.54/0.06
NPO							
Annual	0.10	0.16	−0.18	−0.11	0.44	0.30	−0.19
Autumn	−0.11	0.02	−0.09	−0.03	0.30	0.14	−0.31
Winter	0.33	0.14	0.12	0.16	0.59	−0.30	0.15
Spring	0.15	−0.10	0.14	−0.02	0.39	0.22	−0.19
Summer	−0.13	−0.14	−0.08	0.23	−0.34	0.12	0.22

the surface, but the profiles do converge at midlevels. The largest discrepancies occur at Verkhoyansk (Fig. 2c), with the largest difference at the surface and the profiles remaining quite far apart until 300 hPa where they do converge. Here, the ''surface'' of the nearest model grid point to Verkhoyansk is at about 924 hPa. Verkhoyansk itself is near 1000 hPa and it is reasonable to assert that at least some of the discrepancy is due to the difference in actual topography and location versus the smoothed model topography of the reanalysis. Verkhoyansk is in a narrow valley surrounded on the east, west, and south by mountains. The mountain range directly to the west is quite narrow in the east–west direction, and the horizontal resolution of the model is too large to capture it accurately. The actual flow is from the north as it is channeled around this mountain range. This is evident in the profiles of the observational data, which show a much larger northerly component than the reanalysis data. The reanalysis is not capturing this localized affect, thus explaining the rather large difference in these meridional profiles.

Another concern regarding the 50+ years of NCEP–NCAR reanalysis is that so much of the data predate the modern satellite and Arctic drifting buoy era. Although annual pressure over the Arctic Basin from the reanalysis is in good agreement with observed values throughout the 5-yr period, another test involving the early period is desirable. In Part I of this research (Fig. 15b in Cullather et al. 2000), an average annual spatial depiction of NCEP–NCAR reanalysis MFC truncated to T21 resolution [using the software of Adams and Swarztrauber (1999)] is given for the period 1979–93; this is within the modern satellite and Arctic drifting buoy era. Figure 3 shows that a similar plot using data from 1949 to 1998 yields the same (qualitatively) spatial depiction of MFC over the Arctic Basin. As a consequence, we have confidence in using the 50-yr NCEP–NCAR reanalysis data set to examine the interannual variability of northward moisture flux into the Arctic Basin.

3. Climate indices and Arctic Basin precipitation

a. NAO–AO modulation of Arctic Basin precipitation

Kodera et al. (1999) suggest that the Northern Hemisphere atmospheric circulation in the wintertime related to the NAO can be separated into localized and hemispheric modes of variability. Changes related to the NAO can then be grouped in either mode according to whether they take place within or near the region where data for the NAO index is collected (i.e., within or near the region from the Azores to Iceland) or elsewhere. For example, near-surface air temperatures over eastern Eurasia are more closely associated with the hemispheric NAO mode of variability (Kodera et al. 1999). The NAO index values used here were obtained from the Climate Indices Web site maintained by J. W. Hurrell (http://www.cgd.ucar.edu/cas/climind/nao_winter.html). Thompson and Wallace (1998) define the AO, which is basically a large-scale oscillation of atmospheric mass mostly confined to high- and midlatitude regions of the Northern Hemisphere. The AO appears to be connected to many atmospheric conditions that are typically associated with the NAO, such as the aforementioned surface temperatures over Eurasia (Thompson and Wallace 2000). The AO index values were obtained from D. W. J. Thompson for the time period of January 1949–April 1997 (http://jisao.washington.edu/data/annularmodes/Data/ao_index.html). The AO indices are determined as the leading empirical orthogonal function of sea level pressure (SLP) poleward of 20°N, based on the time period from January 1958 to April 1997 using the NCAR SLP dataset (Trenberth and Paulino 1980). A comparison of NAO and AO indices reveals that they follow each other very closely and that, with very few exceptions, positive (negative) NAO winter index values (December–February) are matched by positive (negative) AO winter indices; correlation is greater than 0.75 for these series. Deser (2000) and Wallace (2000) discussed the similarities between the AO and the NAO, though the authors differed as to which oscillation is dominant. In the

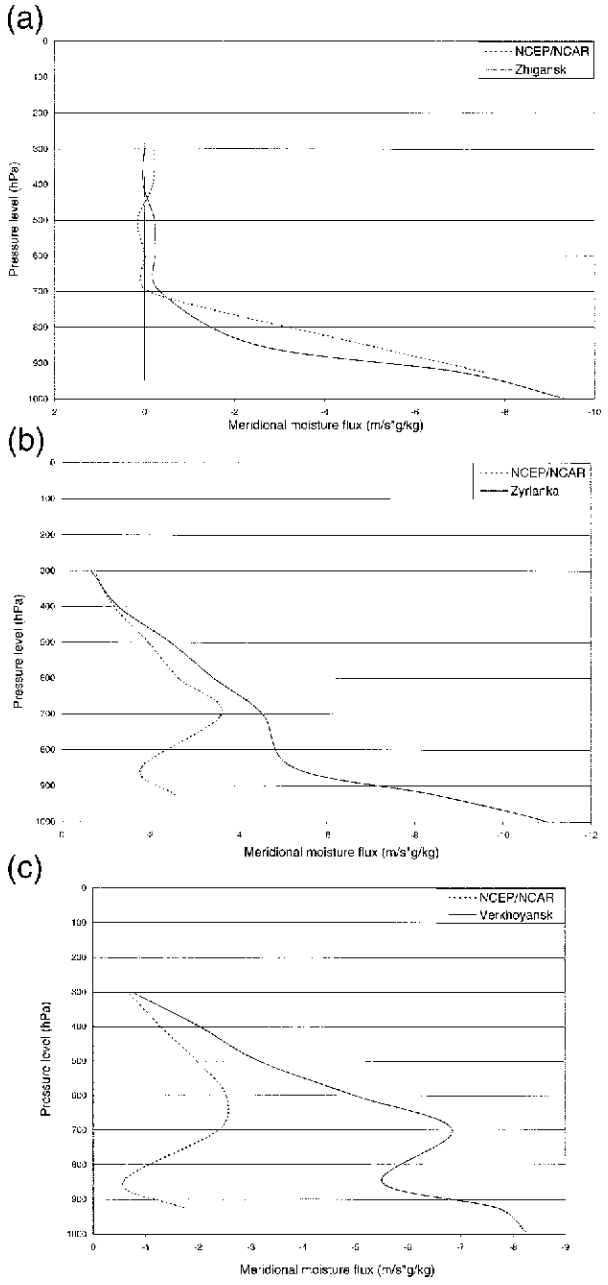

FIG. 2. Average Jul (1979–87) meridional moisture flux profile for the upper-air stations (a) Zhigansk, (b) Zyrianka, and (c) Verkhoyansk in the region bounded by 60°–70° N and 120°–150°E.

following analysis, we focus on the effect the NAO–AO and NPO have on winter precipitation (see Table 1), because these indices are most pronounced in this season. Figure 4 shows the difference field created by subtracting the average winter (December–February) surface pressure for negative NAO winters from that for positive NAO periods using the NCEP–NCAR reanalysis from 1949 to 1999 (winter data for 1949 do not include data from December of 1948). All positive and all negative NAO indices are used, regardless of

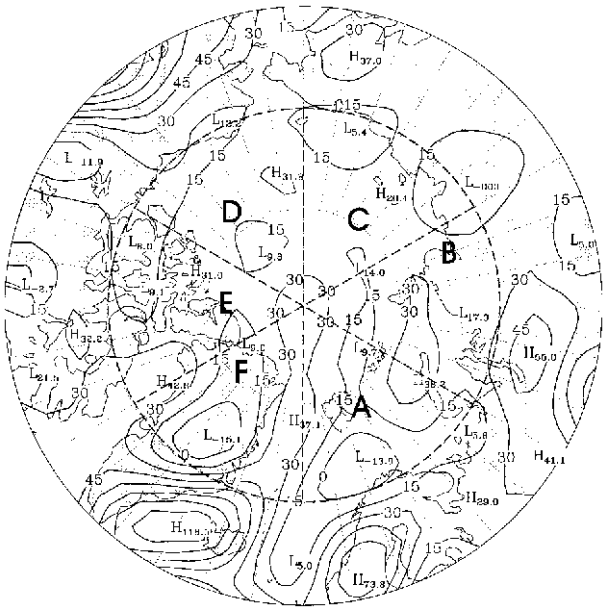

FIG. 3. Average annual spatial depiction of MFC at T21 resolution using the NCEP–NCAR reanalysis data spanning 1949–98. The contour interval is 15 cm yr^{-1}. The dashed lines enclose sectors used to evaluate the regional variability of $P - E$. Sectors are bounded on the south by the 70°N parallel and span 60° long starting eastward from the Greenwich meridian.

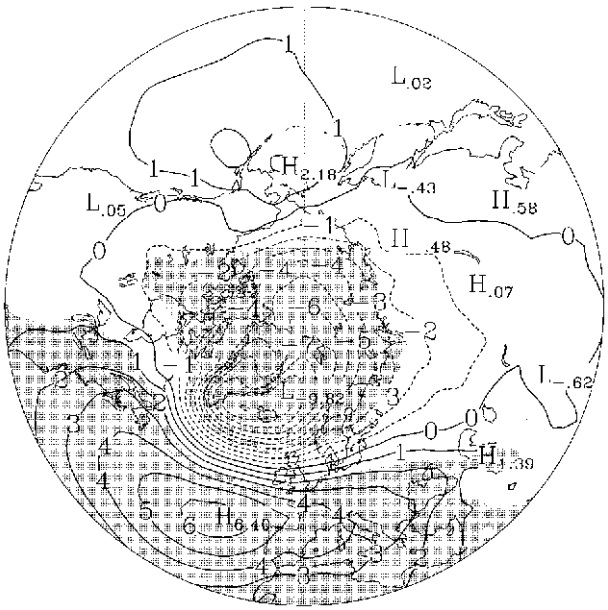

FIG. 4. Difference field obtained by subtracting the average winter (Dec–Feb) surface pressure for negative NAO winter index years from the average winter surface pressure for positive NAO winter index years using NCEP–NCAR reanalysis data from 1949 to 1998. The contour interval is 1 hPa. Areas of statistical significance greater than 95% are shaded.

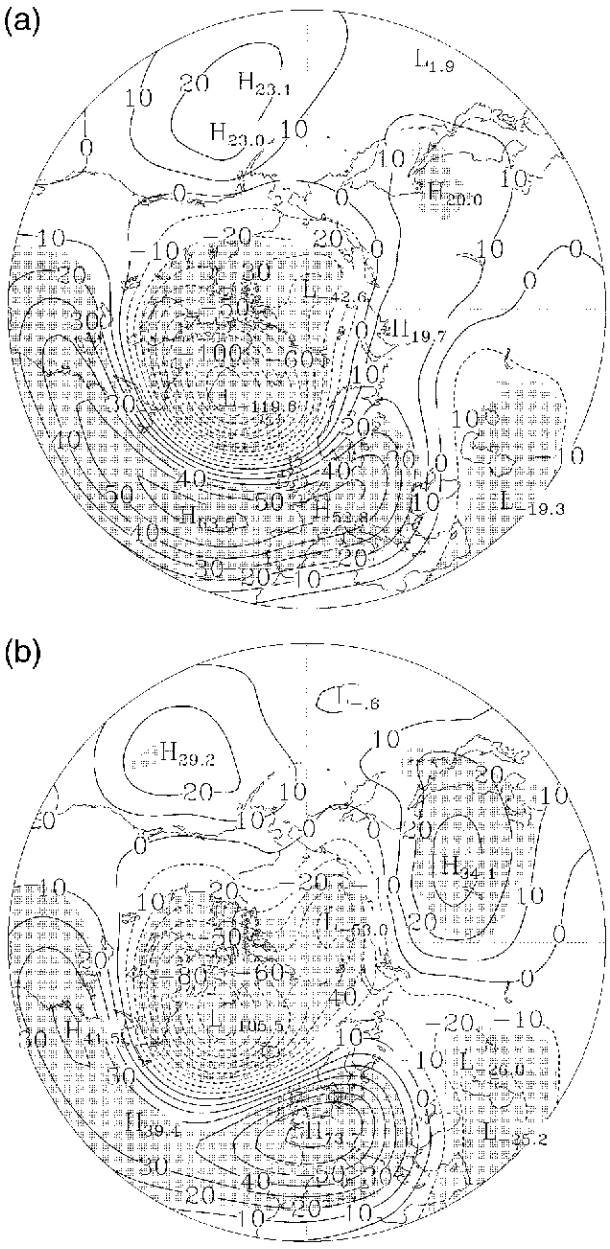

FIG. 5. (a) Same as Fig. 4, but for 500-hPa geopotential height with a contour interval of 10 gpm; (b) same as (a), but using AO winter index values.

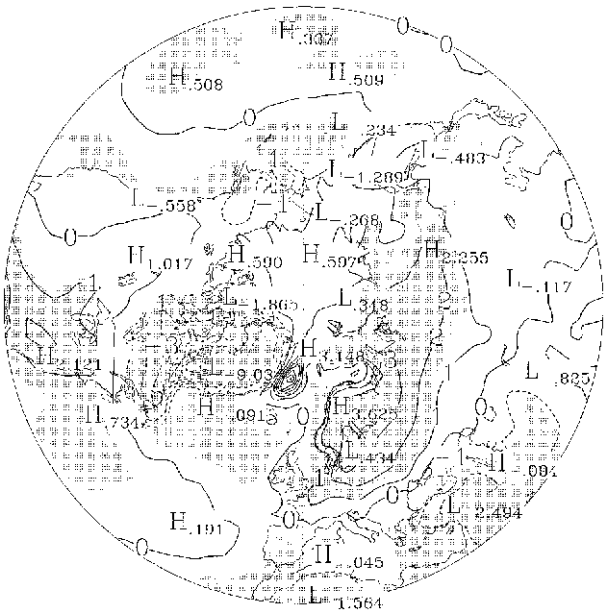

FIG. 6. Same as Fig. 4, but for 2-m temperature with a contour interval of 1°C.

magnitude. The pattern in Fig. 4 reveals an oscillation in atmospheric pressure that is very similar to the first empirical orthogonal function (EOF) of SLP from which the AO is based in Thompson and Wallace (1998, see their Fig. 1, lower-right panel). For the rest of this paper, references to the NAO will mostly be combined with the AO. Shaded on the figure are areas that are statistically significant at greater than the 95% confidence level (Panofsky and Brier 1968, 63–64). The area of large negative values (representing greater surface pressures for negative NAO years) are in the Arctic Basin, with large positive values (representing greater surface pressures for positive NAO years) over the Atlantic Ocean, Europe, and the eastern United States. This structure is consistent with the NAO being a climatic oscillation centered over the North Atlantic Ocean. The corresponding AO pattern is very similar apart from significant negative pressure differences that project far southward from the Arctic Ocean into central Eurasia.

To illustrate how other analysis fields are affected by the NAO–AO, plots similar to Fig. 4 are created for NCEP–NCAR reanalysis 500-hPa geopotential height and 2-m temperature in Figs. 5 and 6, respectively. In Fig. 5a, the 500-hPa geopotential height pattern associated with positive minus negative NAO composites has a slightly more zonal structure to it than the surface pressure pattern (Fig. 4), which tends to weaken over land areas and breaks down entirely over the U.S.–southern Canada portion of North America. In contrast, the 500-hPa geopotential height pattern is more continuous from ocean to land areas, although it is weak to nonexistent over the west coast of the contiguous United States and mostly absent over eastern Asia. In the North Pacific, surface pressure and 500-hPa geopotential height differences are similar in structure, although not statistically significant. Statistical significance analysis shows similar characteristics to Fig. 4 apart from the significant negative values stretching northeast across the Caspian Sea.

Figure 5b presents the 500-hPa geopotential height difference pattern for the AO composites. In broad terms, Figs. 5a and 5b are very similar. The positive differences over the North Atlantic are more discontinuous in Fig. 5b with the dominant center being over

western Europe rather than over the ocean in Fig. 5a. The AO composites are associated with a much more pronounced positive center over eastern Eurasia in Fig. 5b than the NAO composites in Fig. 5a.

Figure 6 provides the average differences in 2-m temperature for positive minus negative NAO composites. The most striking features are the large temperature oscillations around Greenland as well as those over Scandinavia and Siberia. Cooler than average temperatures on the west side of Greenland and warmer temperatures on the east side for positive NAO index winters are consistent with the circulation patterns that are seen in Figs. 4 and 5a, as are the warmer temperatures in Scandinavia and Siberia. During positive NAO index winters, the enhanced troughing over southern Greenland taps the dry, frigid Arctic–northern Canadian air and draws it down the west side of Greenland over Baffin Bay and Davis Strait and even impacts Newfoundland and the Hudson Bay region. By the time it reaches the Labrador Sea to the southwest of Greenland, near-surface air temperatures are modified by oceanic heat fluxes and the temperature signal is greatly attenuated. Additionally, the enhanced North Atlantic easterlies and southerlies bring warm moist flow to the northeastern side of Greenland and Scandinavia, respectively. Surface temperature differences of several degrees between high and low NAO years are seen in these areas. These large temperature differences are also seen in similar plots done for analyses during the modern satellite era and are consistent with work done by Hurrell (1995), who finds warm temperatures over Scandinavia and Eurasia associated with a positive NAO phase. Statistical significance analysis shows the areas of large statistical significance are not quite as uniform as in Figs. 4 and 5. Of interest in this analysis are the areas over northeastern Canada–Greenland and northern Eurasia, which are areas with high statistical significance. A similar plot of 2-m temperature differences for positive minus negative AO composites (not shown) differ from the NAO composites in that there is much more pronounced warming over eastern Eurasia for positive AO winters, consistent with the 500-hPa circulation differences in that area (Fig. 5b compared with Fig. 5a).

Figure 7 shows average differences of forecast $P - E$ for positive minus negative NAO winters using NCEP–Department of Energy (DOE) Atmospheric Model Intercomparison Project (AMIP-2) reanalysis data for 1979–97; the corresponding AO pattern is nearly identical. Reanalysis-2 data are used here because of the spectral noise problems in NCEP–NCAR high-latitude forecast $P - E$. Most striking are the large increases seen in wintertime North Atlantic $P - E$ in the central east region of Greenland and decreases in the southwest region. This pattern is consistent with the 500-hPa geopotential height and near-surface temperature fields in Figs. 5 and 6, which indicate northwesterly flow (mostly cold and dry upper-level flow) on the west side of Greenland and easterly flow (milder and moisture atmospheric conditions) on the northeastern side. Comparison of this plot with the same plot created using ERA-15 data (1979–93) show that they are qualitatively similar, with the ERA-15 plot showing the features over Scandinavia and Greenland much more distinctly. The similarity of $P - E$ results between the different datasets, as well as the location of the largest NAO effect on $P - E$ (southern Greenland/North Atlantic region), further validates the reanalysis dataset.

FIG. 7. Difference field for forecast $P - E$ (contoured every 10 cm yr^{-1}) obtained by subtracting average winter conditions for negative NAO winter index years from the average winter conditions for positive NAO winter index years using NCEP–DOE AMIP-2 reanalysis data from 1979 to 1997. Inlay is the same, but using a 2 cm yr^{-1} contour and for the region of 70°–90°N only.

Another feature of Fig. 7 is the inlay, which is the same as the main part of the figure, but using a 2 cm yr^{-1} contour interval for 70°–90°N only. With this contour interval, we are better able to extract the signal due to the NAO in extreme northern latitudes. Because the Arctic Basin proper is cold and dry, we would not expect to see the large signal we see farther south, where $P - E$ is much higher. However, the enhanced southerly flow along the Scandinavian coast extends into the Arctic Ocean, with increased precipitation for positive NAO years extending along the coast and to the north of it, primarily in the eastern half of the Arctic Basin.

Figure 8 shows the time series of winter NAO and AO indices with winter $P - E$ over the Arctic Basin computed from MFC with mass balance correction and storage changes. Again, winter values are used for analysis because this is when the pressure signal associated with the NAO–AO is strongest. We have included ERA-15 (1979–93) along with the 50 yr of NCEP–NCAR reanalysis to demonstrate the high level of agreement with regards to interannual variability ($r = 0.99$) for

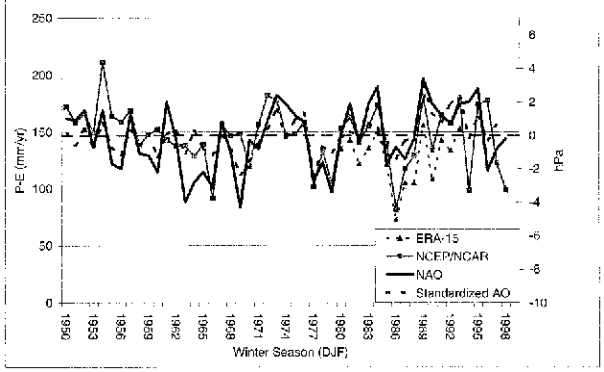

FIG. 8. Winter (Dec–Feb) time series of Arctic Basin NCEP–NCAR reanalysis $P - E$ computed from MFC with the mass balance correction along with winter NAO and standardized AO indices. The ERA-15 (1979–93) $P - E$ is also included.

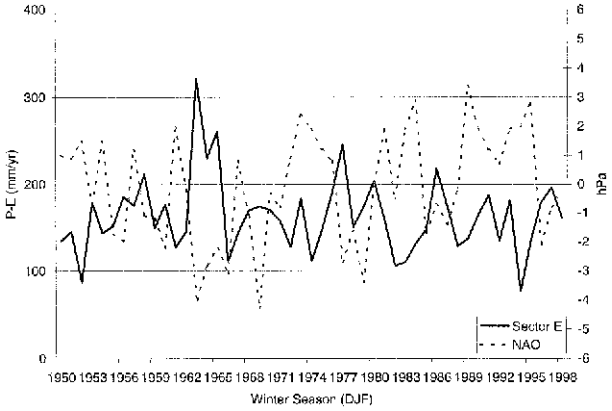

FIG. 9. Computed winter $P - E$ (mm yr^{-1}) for sector E (70°–90°N, 60°–120°W) plotted with the NAO index.

these separately produced datasets. It is also apparent that there are some shared interannual variability characteristics among $P - E$ and the climate indices. Statistical analysis of the winter NAO–AO connection with NCEP–NCAR reanalysis $P - E$ for the entire period (includes only the winter season) in Fig. 8 indicates correlations of 0.49 (NAO:$P - E$) and 0.56 (AO:$P - E$). Using a two-tailed t test, these correlation coefficients are found to be statistically significant at greater than the 99% confidence level after accounting for autocorrelation (see Angell 1981; Quenouille 1952).

A notable feature of Fig. 8 is the stretch of all-positive NAO (and nearly all-positive AO) winter indices starting in 1989 and running through 1995. The number of consecutively positive NAO index winters (representative of lower-than-average pressure from Iceland to the Arctic and/or higher-than-average pressure over/around the Azores) is unprecedented in the earlier period of the series. This feature is obvious in results by Walsh et al. (1996) and from this study in Fig. 1, which shows below-average surface pressure for the Arctic Basin for the same period. In addition to pressure, sea ice for the central Arctic was also affected. Lower-than-average pressure over the Arctic Basin is associated with cyclonic conditions. This was the most recent in a series of cyclonic/anticyclonic periods for the central Arctic, which affects wind-driven ice and ocean motion, as shown by Proshutinsky and Johnson (1997) and Johnson et al. (1999). The $P - E$ values closely mirror the trend of the positive NAO years except in 1994. The AO deviates from the NAO and is negative this year.

As the mean spatial circulation difference characteristics between positive and negative NAO winters in Figs. 4 and 5a suggests, it is likely that certain regions of the Arctic Basin are more directly affected by the oscillating circulation patterns than others. In order to see how subregions of the Arctic Basin are influenced by fluctuations in the NAO–AO, the Arctic Basin is divided into six broad-scale areas consistent with the limited spatial resolution of $P - E$ calculated from MFC (Cullather et al. 2000). Referred to here as sectors A through F, they begin at the prime meridian and are sliced every 60° of longitude to the east (thus sector A is given by 70°–90°N, 0°–60°E; sector B is given by 70°–90°N, 60°–120°E, etc.; see Fig. 3). Table 1 shows correlation analysis results between $P - E$ and the large-scale indices for the entire basin (70°–90°N) and the sectors, on annual and seasonal timescales. Correlations higher than 0.40 are statistically significant at greater than the 99% confidence level using the same procedure as in the total Arctic Basin $P - E$:NAO statistical analysis discussed earlier. Based on correlation analyses of winter $P - E$ with the NAO, sectors A, B, and E are the most strongly tied to the NAO, with correlation values of 0.46, 0.40, and −0.53, respectively. Figure 9 shows sector E (70°–90°N, 60°–120°W) wintertime $P - E$ plotted with the NAO. This plot shows the anticorrelated nature of $P - E$ for sector E to the NAO. This sector, encompassing the Queen Elizabeth and Parry Islands of far northern Canada, is not only anticorrelated with the NAO (and AO) but is also anticorrelated with computed $P - E$ for every other sector in the Arctic Basin. The tendency of sector E wintertime $P - E$ to be anticorrelated with the rest of the Arctic Basin is addressed further in section 4.

Another interesting result from the correlation analysis in Table 1 is that sector C (70°–90°N, 120°–180°E) differs substantially in its level of agreement with the NAO and AO winter index series. The sector C–NAO correlation is only 0.16, whereas the sector C–AO correlation is 0.53. This contrast is consistent with the more pronounced impact of the AO on northeastern Eurasia than the NAO, as illustrated by Fig. 5.

The correlation analysis shows a strong correlation of 0.69 between annual Arctic Basin $P - E$ and annual NAO. Figure 10 shows a plot of annual $P - E$ versus annual NAO, which reveals the strong linear relationship between the two time series. A plot similar to Fig. 7 but for annual precipitation (not shown) reveals that the strongest signal due to the NAO is in the North Atlantic region (east of Greenland and west of Scan-

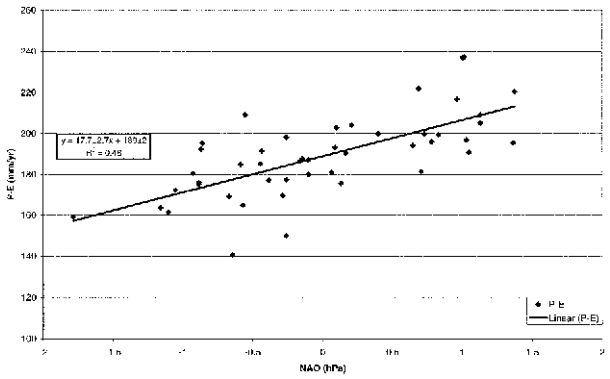

FIG. 10. Annual $P - E$ (mm yr^{-1}) for the Arctic Basin (70°–90°N) vs annual NAO (hPa), including linear regression analysis.

dinavia). This is in agreement with the sector correlation analysis that shows sectors A and F encompassing this area have the highest annual correlations between $P - E$ and the NAO (0.40 and 0.59, respectively, in Table 1).

Table 1 highlights some of the differences between the NAO and AO modulation of Arctic Basin $P - E$. The much higher annual correlation of basin $P - E$ with the NAO (0.69) than the AO (0.49) is consistent with the Atlantic Ocean domination of the northward poleward moisture flux across 70°N discussed by Serreze et al. (1995), Cullather et al. (2000), and Dickson et al. (2000). There is also a seasonal contrast between the NAO and AO modulation of $P - E$ for the Arctic Basin. The NAO correlations are largest for autumn, winter, and spring, while the AO correlations are largest for winter, spring, and summer.

b. NPO and Arctic Basin precipitation

Figure 4 shows that the NAO–AO has a weak and statistically insignificant impact on the winter pressure field over the North Pacific during the period of the NCEP–NCAR reanalysis. Another oscillation, the NPO, exists for the North Pacific high–midlatitudes and is monitored by the North Pacific index (Trenberth 1990). Trenberth (1990) showed that it is closely tied with the Pacific–North American (PNA) teleconnection pattern. Although originally spanning a greater region on the North Pacific, the index is currently composed of an area-weighted sea level pressure over the region 30°–60°N, 160°E–140°W (Trenberth and Hurrell 1995). Trenberth and Hurrell (1995) show that the oscillations are greatest in the middle of winter. Here, differences of composites similar to those in Figs. 4–7 are carried out for positive and negative NPO (relative to the mean winter regional sea level pressure) winters. (North Pacific oscillation indexes obtained from Climate Indices Web site, maintained by J. W. Hurrell.) Figures 11a and 11b show difference composites of 500-hPa geopotential height and 2-m temperature for positive minus negative NPO winters, respectively. Within the domain of Fig. 11a (30°N to the Pole), it is possible to see some of the effects of the PNA teleconnection, starting with the large positive 500-hPa geopotential height signal over the North Pacific (centered 10°–15° south of the Aleutian chain) to the signal (opposite sign) over western Canada and, last, one over the mid-Atlantic coast–southeast United States (same sign). A similar pattern emerges in near-surface temperatures of Fig. 11b. Wintertime temperatures from the NPO-PNA signal are shown to vary just under a degree at the peak of variation in the North Pacific, 1°–2° over the southeastern United States, and nearly 4° in northwestern Canada–southeastern Alaska. The sign of warmer (cooler) temperatures over the North Pacific and southeast United States and cooler (warmer) temperatures in western Canada and the west coast region of the United States using NCEP–NCAR reanalysis matches that found by Trenberth and Hurrell (1995). Statistical significance greater than the 95% confidence level is shaded on this

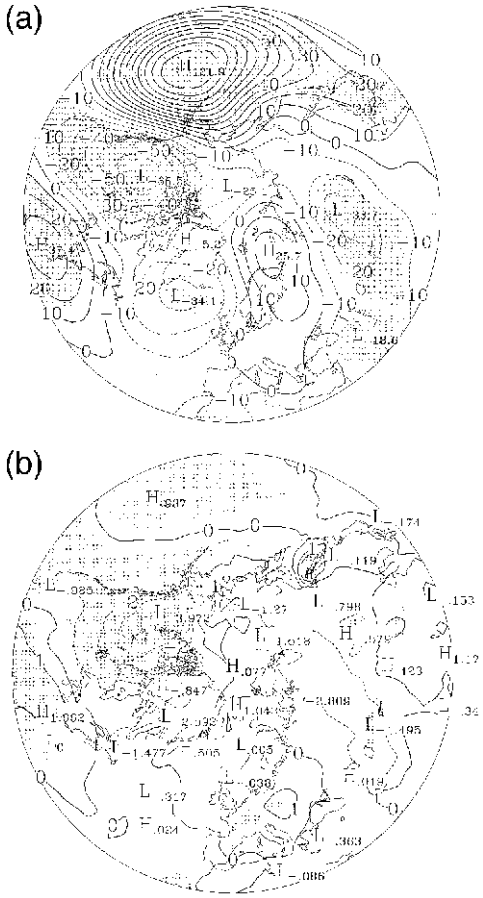

FIG. 11. Difference fields for (a) 500-hPa geopotential height (contour interval is 10 geopotential meters) and (b) 2-m temperature (contour interval is 1°C) obtained by subtracting average winter conditions (Dec–Feb) for negative NPO winter index years from the average winter conditions for positive NPO winter index years using NCEP–NCAR reanalysis data from 1949 to 1998.

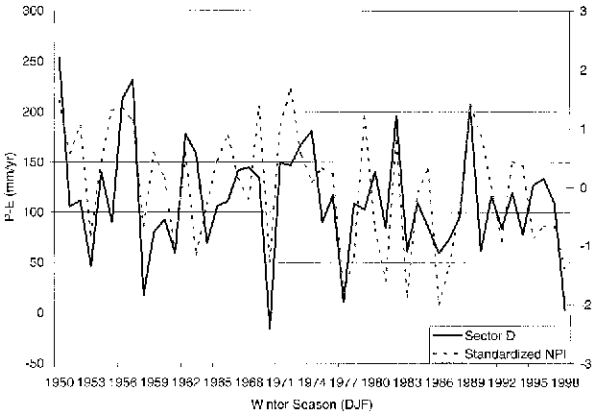

FIG. 12. Standardized North Pacific index based on winter (DJF) surface pressures plotted with sector D computed $P - E$ (mm yr^{-1}).

figure as it was on Figs. 5 and 6. The areas of greatest statistical significance are over the North Pacific, and United States–Canada. These are the regions where the North Pacific oscillation would be expected to have the greatest impact. Again, the temperature difference plot is less uniform as it was for the NAO–AO figures.

Because the main NPO-based signals in 500-hPa geopotential height and 2-m temperature over the Arctic Basin are largest for the periphery (Fig. 11), the individual sectors of Arctic Basin $P - E$ are evaluated with regard to their winter connection to the NPO. The sectors are the same as those in section 3a, sectors A–F. Correlation analysis of each sector with the North Pacific index reveals that sector D (70°–90°N, 120°–180°W) computed $P - E$ has the highest statistically significant correlation with a value of 0.59 (see Table 1). This compares with an overall Arctic Basin–North Pacific index correlation value of 0.33. Figure 12 shows the time series of the standardized North Pacific index based on winter [December–February (DJF)] surface pressures with $P - E$ for sector D, and illustrates that for most years the agreement is close. This sector spans the region that is strongly influenced by the NPO in Fig. 11. As is the case with the NAO and AO, the NPO is positively correlated with every sector except for sector E (correlation $= -0.30$). Section 4 looks at this finding from the point of view of annual running mean meridional moisture flux across 70°N.

Apart from sector D, the North Pacific index is weakly correlated with sector $P - E$ for all seasons.

4. Regional variations in moisture flux across 70°N for the past 50 years

a. General characteristics

In order to demonstrate the major regional variations in moisture transport across the Arctic Basin, Fig. 13 shows a contour plot of 12-month running mean meridional atmospheric moisture transport across 70°N by longitude for the 50 yr of the NCEP–NCAR reanalysis. The most consistent and dominant features present are the dark green line of large positive moisture flux between 300° to 315°E (45° and 60°W) and the low (near zero) values just to the east. The former region covers the Davis Strait and western Greenland coastline. The effects of positive (northward) moisture flux through this region are exhibited in the spatial depiction of MFC in Fig. 3. The consistent low values just to the east include the Greenland Ice Sheet, a topographic feature that acts as an effective moisture transport barrier. This feature is also noticeable in Fig. 3, with large positive MFC values along the southeastern Greenland coastline to a near-zero values inland at 70°N.

Another prominent feature in Fig. 13 is the wide, fairly continuous region of negative flux across 70°N (blue) between 230° and 280°E (80° and 130°W). In Part I of this study (Cullather et al. 2000), it was shown how this region was the only source of substantial negative meridional (i.e., out of the Arctic Basin) moisture transport (see their Fig. 8). This is also the part of northern Canada that approximately corresponds with the southern boundary of sector E, a sector that earlier in the paper is shown to have wintertime computed $P - E$ that is negatively correlated with every other sector of Arctic Basin $P - E$. In fact, though the correlation signal is negative with the climate indices addressed in this paper, it is stronger than that of any other sector with regard to its connection to the NAO, with over 28% of its wintertime variance in $P - E$ tied to the NAO. It is also the only sector that is negatively correlated with the North Pacific index. As there is almost no shared variance between the NPO and the NAO (near zero) or even between the NPO and the AO (variance less than 3% based on a correlation over almost 50 yr of 0.17), the 10% shared variance we find between sector E wintertime $P - E$ and the NPO is mostly independent of the NAO–AO fluctuations. This means that nearly 40% of the variance in winter $P - E$ for sector E is related to the NAO and NPO.

Also prominent in Fig. 13 is a rather unusual region of negative flux near 120°E from the beginning of the series in 1949 to about 1955. It arouses special interest due to the magnitude and duration of this transport feature and the abruptness with which it ends. It also happens to occur only in the earliest part of our series. In Fig. 4c of Trenberth and Paolino (1980), mean pressure discontinuities (relative to the period 1956–77) are shown to exist near and around this region from the mid-1940s to the mid-1950s, especially during the summer–autumn half year. This suggests that early period data for this region lacked accuracy and/or suffered from low density of data collection sites. Given that Fig. 13 is constructed using NCEP–NCAR reanalysis data, we look now at some of the collected data for the region that was available to the reanalysis. Figure 14 provides the time series of the number of observations per month averaged over every 2.5° × 2.5° lat–long grid box for the region spanning 60°–90°N, 90°–150°E that went into

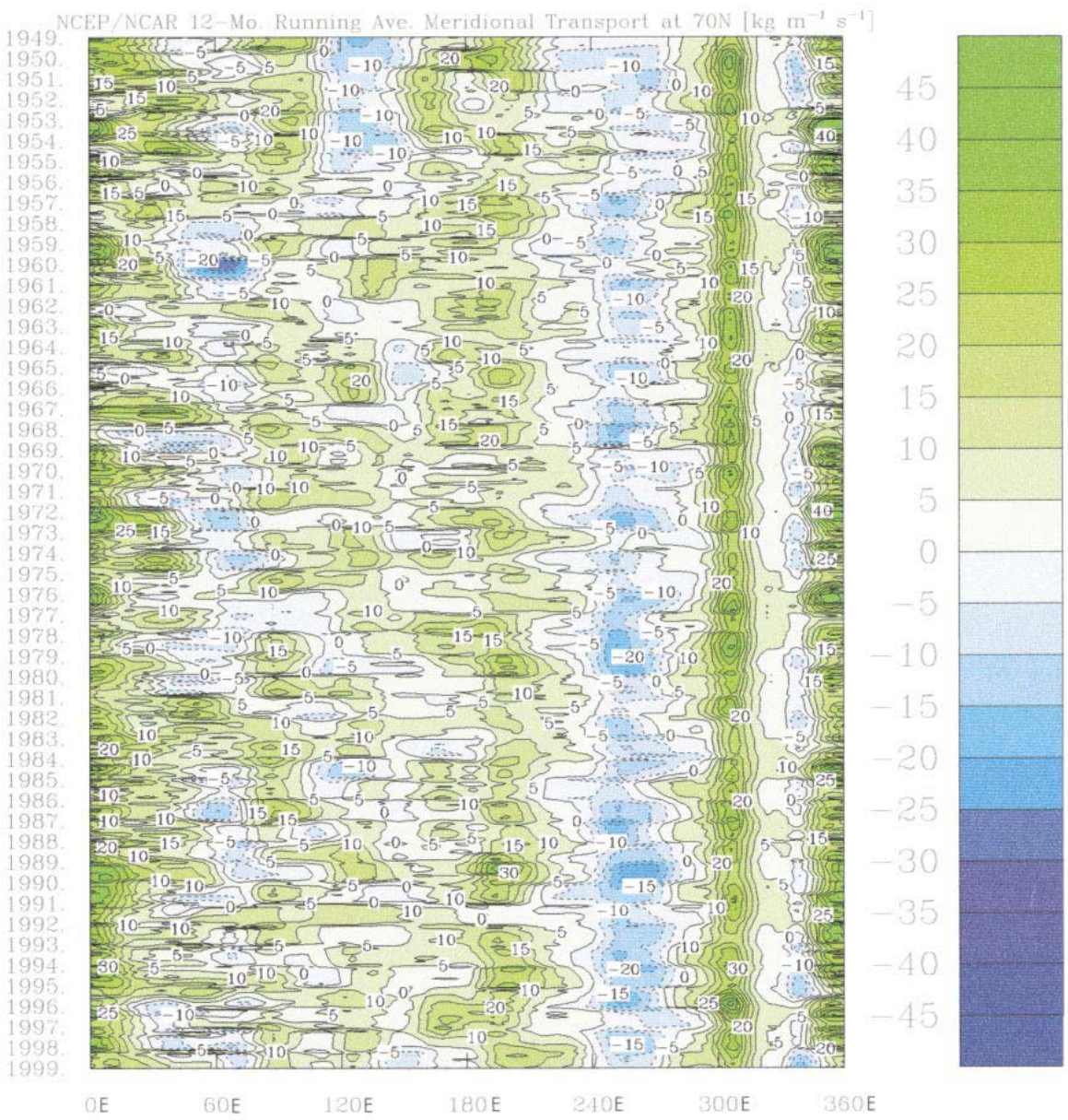

FIG. 13. The 12-month running mean meridional atmospheric moisture transport across 70°N (kg m^{-1} s^{-1}) by longitude for the 50 yr of the NCEP–NCAR reanalysis (long on the *x* axis are degrees east).

the reanalysis for both surface and upper-air (radiosonde, dropsonde, and pibal) data (http://wesley.wwb.noaa.gov/reanalysis.html). From the beginning of the period to about 1955, surface observations remain steady at around 17 observations per month per grid box. Upper-air observations increase from almost nothing to around 3 by 1952, remaining near 3 from 1952 to 1955. After 1955, the number of surface and upper-air observations that are available to the reanalysis jumps by 50% or more. For the most part, the observation frequency in the reanalysis for this sector remains above the pre-1955 level throughout the time prior to the modern satellite era. The only major exception occurs around 1958, when surface observations plummet to near zero. The fact that poleward moisture flux becomes negative again around this time near 120°E may or may not be related, although even brief (~year) periods of negative moisture flux are rare in this location for the 50 yr studied. Because of the limited data available for use in the NCEP–NCAR reanalysis for the region studied here, it is difficult to assign great significance to the anomalous negative flux feature near 120°E from 1949 to 1955 in Fig. 13.

Further inspection of Fig. 13 shows high interannual variability of moisture flux across 70°N between 60° and 120°E (i.e., the southern boundary of sector B).

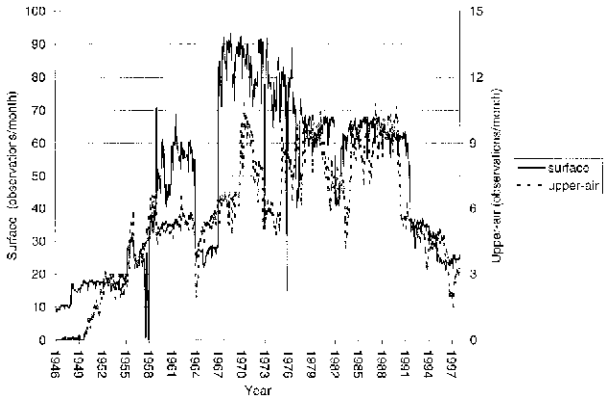

FIG. 14. Time series of observations per month averaged over every 2.5° × 2.5° lat–long grid for the region 60°–90°N, 90°–150°E that went into the NCEP–NCAR reanalysis for surface (solid line) and upper-air (dashed line) data.

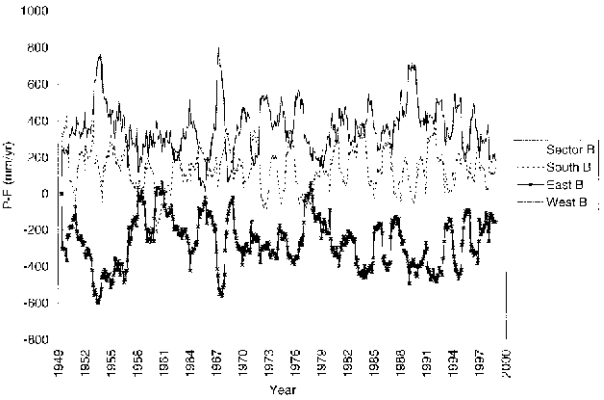

FIG. 15. Annual running mean moisture transport (at monthly intervals) into sector B (70°–90°N, 60°–120°E) across the southern (dashed line), eastern (starred line), and western (thin solid line) boundaries, as well as the total (thick solid line) annual running mean MFC for sector B.

Although there are periods of negative moisture flux across the region, values are mostly positive. This sign preference is more easily conveyed by the dashed line in Fig. 15, which shows the annual running mean moisture transport (at monthly intervals) across 70°N for sector B. Figure 15 also shows the east (starred line) and west (thin solid line) annual running mean moisture transports into sector B, as well as the total annual running mean computed MFC; with the mass balance correction increasing the annual MFC by only 11%, the uncorrected MFC discussed here nearly equals $P - E$. The anticorrelated nature of sector B east and west boundary moisture fluxes (-0.71) suggests large zonal moisture transports (relative to meridional and total moisture flux) through the sector. Despite considerable interannual variability in moisture flux from all three sector boundaries, the interannual variability of total computed MFC to sector B is surprisingly small by comparison, hovering around to just above 200 mm yr^{-1}. Although the absolute magnitude of the south boundary contribution to sector B MFC is usually smaller than those of the east and west boundaries, its value is often close to that of total sector B MFC. Section 4b addresses the variations in meridional moisture transport across this boundary for the summertime, climatologically the period of greatest atmospheric moisture flux for the region.

b. Interannual variability of meridional summertime moisture flux over western Siberia

In a previous study by Bromwich et al. (2000), a region of large summertime moisture transport variability was identified over western Siberia, east of the Urals, associated with the timing and development of the Urals trough. In their Fig. 19, they separated years of large positive July moisture flux across 70°N between 60° and 120°E (i.e., the southern boundary of sector B) from years of low or negative July moisture transport and plotted vertically integrated moisture fluxes for the two scenarios using ERA-15 (1979–93). The results suggested an opposing summertime circulation regime, with high (low) poleward summer moisture transports over the west Siberian plain during low (high) poleward summer moisture transports over Scandinavia. Their analysis is here extended in time and amplified in scope using the 50-yr NCEP–NCAR reanalysis. The data were separated into years in which the average moisture flux across 70°N was greater than the median value (large poleward flux) and years in which it was less (low or negative poleward flux). Included is an evaluation of the differences of surface pressure, 500-hPa geopotential height, and surface temperature between high and low July poleward flux regimes.

Figure 16 shows the average vertically integrated moisture fluxes for July from the NCEP–NCAR reanalysis for (a) years of large west Siberian plain poleward flux (21 out of 50 total) and (b) years of low or negative regional poleward flux (29 out of 50 total). These composite plots based on 50 yr of the NCEP–NCAR reanalysis are very similar to those produced using the ERA-15 in Fig. 19 of Bromwich et al. (2000). The presence of this pattern in a 50-yr dataset in addition to the 15-yr dataset is a much more robust confirmation of the pattern. It is apparent from Fig. 16b that Julys with low/negative poleward flux exhibit a clear southwesterly character near the southwest corner of Scandinavia that extends northeast to influence the Barents Sea and regions beyond. The pattern in Fig. 16a during Julys with large poleward flux across 70°N for the west Siberian plain shows quite a different picture over Scandinavia, with a much more zonal character to the moisture transport. In addition, we infer from Fig. 16a that the southwest corner of sector B appears to be affected by enhanced troughing to the west, while the southeast corner appears to be affected by enhanced ridging to the east, as compared with Fig. 16b. In order to more

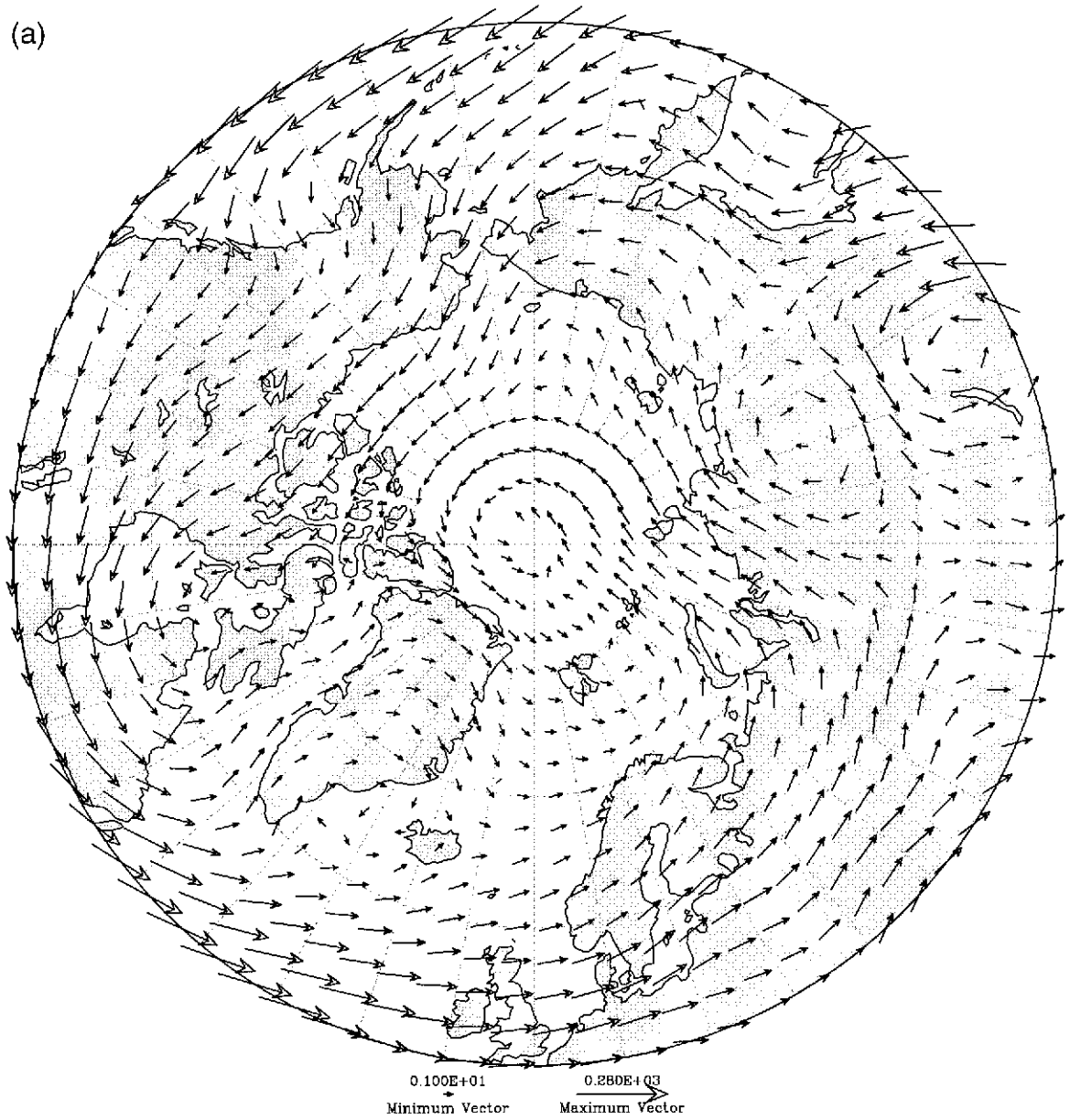

FIG. 16. The spatial depiction of average vertically integrated Jul moisture flux from the NCEP–NCAR reanalysis for years of (a) large and (b) low or negative Jul poleward moisture transport across 70°N for the west Siberian plain (60°–120°E).

clearly see the differences in ridging–troughing patterns between the composite July moisture flux plots in Fig. 16, differences of the composites of Julys with high and low/negative moisture transport for 500-hPa geopotential height are plotted in Fig. 17 (high-poleward-moisture-flux Julys minus low/negative-poleward-flux Julys). It clearly shows significant troughing and ridging patterns at the southwest and southeast corners of sector B, respectively, as are inferred by the depictions of vertically integrated moisture transports in Fig. 16. The significant negative differences in Fig. 17 south of Hudson Bay and adjacent to the Labrador Sea are associated with amplified 500-hPa troughs at the time of high July poleward moisture transport over the west Siberian plain. A similarly constructed surface pressure plot (not shown) shows statistically significant features shifted eastward relative to those over the west Siberian plain in Fig. 17. This suggests baroclinic conditions with warm air advection to the east and cold air advection to the west. A plot of surface temperature composite differences for high minus low July poleward moisture transport periods (not shown) supports this contention.

Last, the importance of summertime poleward moisture transport in this region is demonstrated in Fig. 18. This figure shows the average annual cycle of moisture flux across the southern boundary of sector B for years

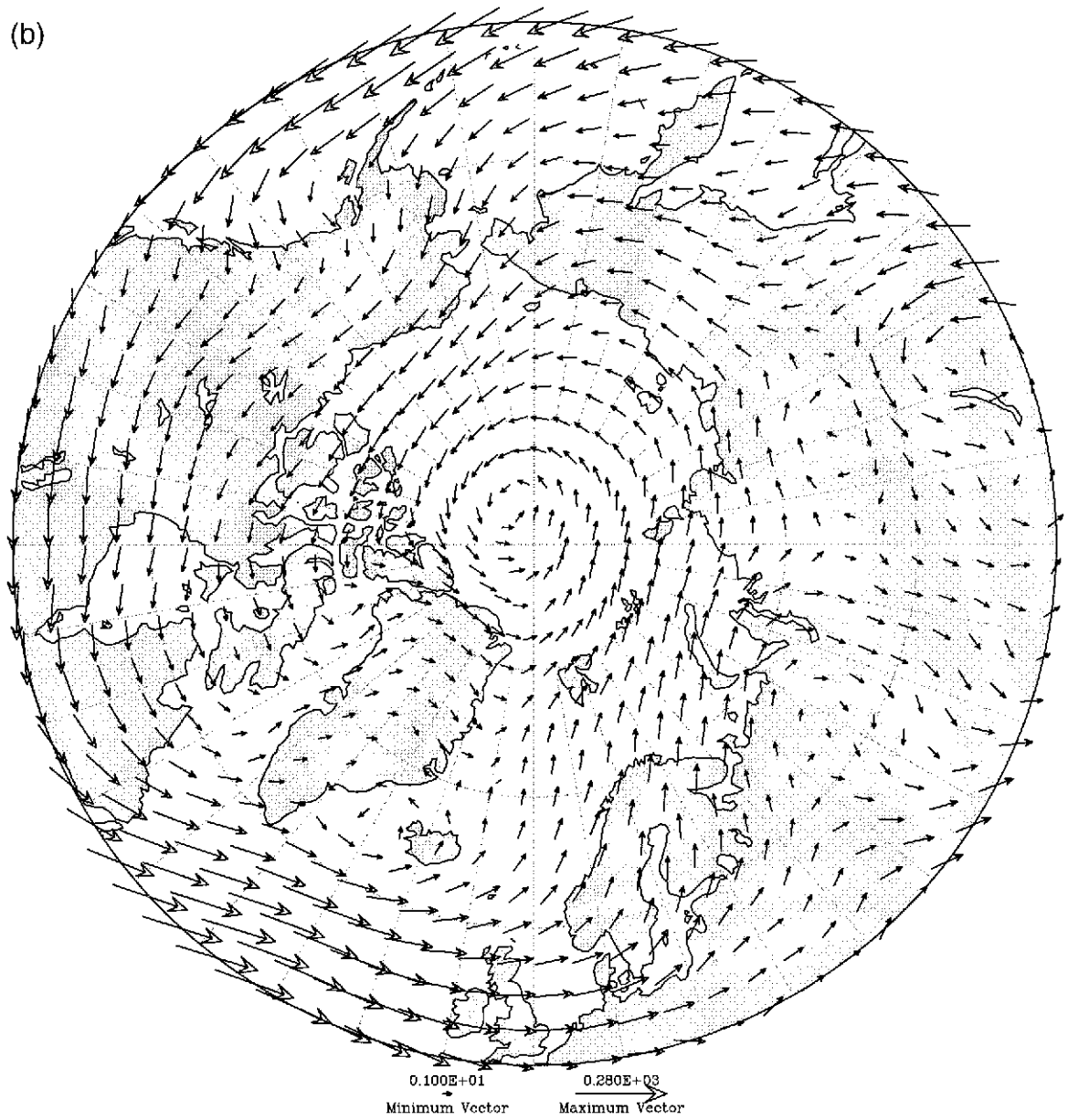

FIG. 16. (*Continued*)

of high July poleward moisture flux (diamond line—annual cycle for 44% of the 50 NCEP–NCAR reanalysis years) and for years of low or negative July poleward moisture flux (hollow square line). Major differences in other months based on the July poleward flux separation do not exist. Inspection of regional 500-hPa geopotential height patterns (not shown) demonstrates no substantial difference between the two July moisture flux scenarios in the months preceding and following July, with the possible exception of June. We do not see this circulation pattern when the other months of the year are stratified according to the same criteria (years with larger than the median value and years that are less than the median value). Because a majority of poleward moisture flux occurs between June and September in this sector (68% of the annual total), the variability in July poleward flux makes a 70% difference to the annual poleward flux to the Arctic Basin between 60° and 120°E.

5. Discussion

Results presented in this paper using the 50-yr NCEP–NCAR reanalysis to gauge atmospheric variability associated with the AO, NAO, and NPO are consistent with those found in previous studies as referenced in section 3. Further, it is found that these oscillations do significantly impact computed $P - E$ for the Arctic

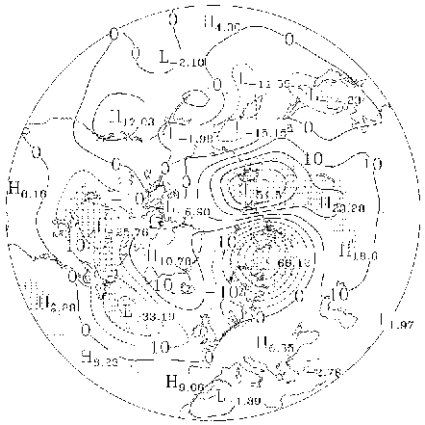

FIG. 17. The difference of average 500-hPa geopotential height patterns for Julys with high and low (or negative) poleward moisture transport (high minus low/negative) across 70°N for the west Siberian plain (60°–120°E). The contour interval is 10 geopotential meters (areas of statistical significance greater than 95% shaded).

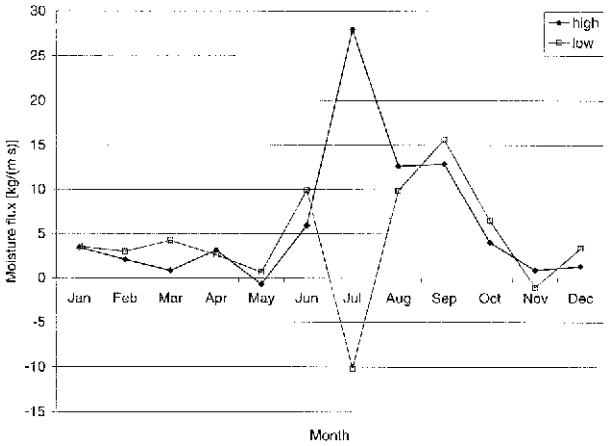

FIG. 18. The annual cycle of moisture flux across 70°N for the west Siberian plain (60°–120°E) for years of high Jul poleward moisture flux (diamond line) and for years of low or negative Jul poleward moisture flux (hollow-square line).

Basin. The recent anomalous positive NAO period from 1988 to 1995 is well matched by higher-than-average NCEP–NCAR reanalysis Arctic Basin $P - E$ for most of these years (winter and annual). It is shown that atmospheric fluctuations associated with the NAO and hemispheric-scale AO are strongly related. These fluctuations are highly associated with variability in wintertime $P - E$ for the Arctic Basin regions given by 70°–90°N, 0°–120°E (sectors A and B) and 70°–90°N, 60°–120°W (sector E). The only instance of significant difference between the correspondence of NAO and AO with $P - E$ occurs in sector C (70°–90°N, 120°–180°E). Here, the connection in computed $P - E$ and the AO is substantially more significant than the NAO for every season except summer; this result arises from the much more pronounced impact of the hemispheric-scale AO signal in northeastern Eurasia. On an annual basis, Arctic Basin $P - E$ is much more closely correlated with the NAO (0.69) than the AO (0.49), consistent with the Atlantic Ocean domination of the northward moisture flux across 70°N.

Arctic Basin $P - E$ is also found to be weakly correlated with the NPO during winter (and to the PNA teleconnection, which is almost perfectly anticorrelated with the NPO index). The exception is the region from 70°–90°N, 120°W–180° (sector D) throughout the year, with a notable correlation between computed winter $P - E$ and the NPO index of 0.59. This region includes the north Alaskan coastline and Beaufort Sea.

For the NAO–AO and NPO, only one region, given by 70°–90°N, 60°–120°W (sector E) had computed winter $P - E$ that was antiphase with these oscillations. Between them, the NAO–AO and NPO account for nearly 40% of the variance in sector E wintertime $P - E$. This region corresponds with the only region of consistently negative annual running-mean moisture flux. Another important feature studied in section 4 is the high mode of variability in summertime moisture flux across 70°N over western Siberia, associated with the southern boundary of sector B. Its importance is closely tied to the fact that most poleward moisture transport for this region occurs during the summer months. Its highly variable nature from one year to the next leads us to look for similarly varying patterns in other fields. The most telling results were found in 500-hPa difference fields created by taking the average pattern during large positive poleward moisture transport Julys and subtracting the average 500-hPa pattern during negative moisture transport Julys. The results using 50 yr of NCEP–NCAR reanalyses support a previous study by Bromwich et al. (2000) suggesting an opposing summertime circulation regime for western Siberia and Scandinavia. The circulation yields high (low) poleward summer moisture transports over the west Siberian plain during low (high) poleward summer moisture transports over Scandinavia associated with the location of a ridge to the east (west) of the west Siberian plain. The ubiquitous nature of this ridge and the corresponding zonal extent of the Urals trough (both specifically here for July) do not appear to be directly related to variability in the primarily wintertime phenomena of the NAO–AO or the NPO.

The findings presented in this study demonstrate a key aspect of Arctic Basin $P - E$. Large-scale hemispheric modes of (surface pressure based) variability in the atmosphere seen in the NAO, AO, and NPO show fairly consistent but regionally varying relationships in comparison to other fields. This is clearly shown for sector computed $P - E$. While most sectors exhibit a similar correspondence with these atmospheric oscillations, sector E showed a strong inverse relationship to that in neighboring sectors during winter.

Acknowledgments. This research is supported by the National Aeronautics and Space Administration via

Grant NAG5-6001 and by the National Science Foundation via Grants OPP-9907549 and OPP-9910334, all to the second author. Reanalysis data were obtained from the National Center for Atmospheric Research. We thank John Walsh and an anonymous reviewer for their helpful comments.

REFERENCES

Adams, J. C., and P. N. Swarztrauber, 1999: SPHEREPACK 3.0: A model development facility. *Mon. Wea. Rev.,* **127,** 1872–1878.

Alestalo, M., 1983: The atmospheric water vapor budget over Europe. *Variations in the Global Water Budget,* A. Street-Perrott, M. Beran, and R. Ratcliffe, Eds., D. Reidel, 67–79.

Angell, J. K., 1981: Comparison of variations in atmospheric quantities with sea surface temperature variations in the equatorial eastern Pacific. *Mon. Wea. Rev.,* **109,** 230–243.

Broecker, W. S., 1997: Thermohaline circulation, the Achilles heel of our climate system, will man-made CO_2 upset the current balance? *Science,* **278,** 1582–1588.

Bromwich, D. H., R. I. Cullather, and M. C. Serreze, 2000: Reanalysis depictions of the Arctic atmospheric moisture budget. *The Arctic Ocean Fresh Water Budget,* E. L. Lewis, Ed., Kluwer Academic, 163–196.

Chapman, W. L., and J. E. Walsh, 1993: Recent variations in sea ice and air temperature in high latitudes. *Bull. Amer. Meteor. Soc.,* **74,** 33–47.

Cullather, R. I., D. H. Bromwich, and M. L. van Woert, 1998: Spatial and temporal variability of Antarctic precipitation from atmospheric methods. *J. Climate,* **11,** 334–368.

——, ——, and M. C. Serreze, 2000: The atmospheric hydrologic cycle over the Arctic Basin from reanalyses. Part I: Comparison with observations and previous studies. *J. Climate,* **13,** 923–937.

Deser, C., 2000: On the teleconnectivity of the ''Arctic oscillation.'' *Geophys. Res. Lett.,* **27,** 779–782.

Dickson, R. R., and Coauthors, 2000: The Arctic Ocean response to the North Atlantic oscillation. *J. Climate,* **13,** 2671–2696.

Gibson, J. K., P. Kållberg, S. Uppala, A. Hernandez, A. Nomura, and E. Serrano, 1997: ERA description. ECMWF Re-Analysis Project Report Series 1, 72 pp. [Available from ECMWF, Shinfield Park, Reading RG2 9AX, United Kingdom.]

Goeber, M., R. Hagenbrock, A. Hense, and F. Ament, 2000: Comparison of atmospheric budgets based on radiosonde and reanalysis data on the same grid: An Arctic example. *Proc. Second WCRP Int. Conf. on Reanalyses,* Wokefield Park, United Kingdom, World Climate Research Programme, 233–240.

Hurrell, J. W., 1995: Decadal trends in the North Atlantic oscillation: Regional temperatures and precipitation. *Science,* **269,** 676–679.

Johnson, M. A., A. Y. Proshutinsky, and I. V. Polyakov, 1999: Atmospheric patterns forcing two regimes of Arctic circulation: A return to anticyclonic conditions? *Geophys. Res. Lett.,* **26,** 1621–1624.

Kalnay, E., and Coauthors, 1996: The NCEP/NCAR 40-Year Reanalysis Project. *Bull. Amer. Meteor. Soc.,* **77,** 437–471.

Kodera, K., H. Koide, and H. Yoshimura, 1999: Northern Hemisphere winter circulation associated with the North Atlantic oscillation and stratospheric polar-night jet. *Geophys. Res. Lett.,* **26,** 443–446.

Maslanik, J. A., M. C. Serreze, and R. G. Barry, 1996: Recent decreases in Arctic summer ice cover and linkages to atmospheric circulation anomalies. *Geophys. Res. Lett.,* **23,** 1677–1680.

Overpeck, J., and Coauthors, 1997: Arctic environmental change of the last four centuries. *Science,* **278,** 1251–1256.

Panofsky, H. A., and G. W. Brier, 1968: *Some Applications of Statistics to Meteorology.* The Pennsylvania State University, 223 pp.

Proshutinsky, A., and M. Johnson, 1997: Two circulation regimes of the wind-driven Arctic Ocean. *J. Geophys. Res.,* **102,** 12 493–12 514.

Quenouille, M. H., 1952: *Associated Measurements.* Butterworths, 241 pp.

Serreze, M. C., and C. M. Hurst, 2000: Representation of mean Arctic precipitation from NCEP–NCAR and ERA reanalyses. *J. Climate,* **13,** 182–201.

——, J. D. Kahl, and S. Shiotani, 1992: The Historical Arctic Rawinsonde Archive documentation manual. Special Rep. 2, National Snow and Ice Data Center, University of Colorado, 26 pp. [Available from NSIDC, Campus Box 449, University of Colorado, Boulder, CO 80309–0449.]

——, R. G. Barry, and J. E. Walsh, 1995: Atmospheric water vapor characteristics at 70°N. *J. Climate,* **8,** 719–731.

——, F. Carse, R. G. Barry, and J. C. Rogers, 1997: Icelandic low cyclone activity: Climatological features, linkages with the NAO, and relationships with recent changes in the NH circulation. *J. Climate,* **10,** 453–464.

Thompson, D. W. J., and J. M. Wallace, 1998: The Arctic oscillation signature in the wintertime geopotential height and temperature fields. *Geophys. Res. Lett.,* **25,** 1297–1300.

——, and ——, 2000: Annular modes in the extratropical circulation. Part I: Month-to-month variability. *J. Climate,* **13,** 1000–1016.

Trenberth, K. E., 1990: Recent observed interdecadal climate changes in the Northern Hemisphere. *Bull. Amer. Meteor. Soc.,* **71,** 988–993.

——, and D. A. Paolino Jr., 1980: The Northern Hemisphere sea-level pressure data set: Trends, errors and discontinuities. *Mon. Wea. Rev.,* **108,** 855–872.

——, and J. W. Hurrell, 1995: Decadal climate variations in the Pacific. *Natural Climate Variability on Decade-to-Century Time Scales,* D. G. Martinson, Ed., National Academy Press, 472–481.

van Loon, H., and J. C. Rogers. 1978: The seesaw in the winter temperatures between Greenland and northern Europe. Part I: General description. *Mon. Wea. Rev.,* **106,** 296–310.

Wallace, J. M., 2000: North Atlantic oscillation/annular mode: Two paradigms–one phenomenon. *Quart. J. Roy. Meteor. Soc.,* **126,** 791–805.

Walsh, J. E., W. L. Chapman, and T. L. Shy, 1996: Recent decrease of sea level pressure in the central Arctic. *J. Climate,* **9,** 480–486.